

Understanding the Limitations of Charge Transporting Layers in Mixed Lead–Tin Halide Perovskite Solar Cells

Kaicheng Zhang, Karen Forberich, Larry Lüer, José Garcia Cerrillo, Wei Meng, Xiaoyan Du, Vincent M. Le Corre, Yicheng Zhao, Tianqi Niu, Qifan Xue, L. Jan Anton Koster, Ning Li,* and Christoph J. Brabec*

Lead–tin (Pb/Sn) mixed perovskites are considered as promising photovoltaic materials owing to their adjustable bandgap and excellent optoelectronic properties. The low-bandgap perovskite solar cells (PSCs) based on lead–tin mixed perovskites play a critical role in the overall performance of perovskite-based tandem devices. Nevertheless, the current record efficiencies for Pb/Sn PSCs are mostly reported in devices with p–i–n configuration rather than n–i–p, which restricts the further development of conventional perovskite-based tandem solar cells. Herein, this work systematically investigates the influence of the interlayers on the performance of low-bandgap PSCs by analyzing the energy losses in both n–i–p and p–i–n devices. Quasi-Fermi level splitting (QFLS) analysis of pristine films and films covering charge extraction layers reveals that the electron transport layer/perovskite interface is dominating the V_{OC} losses. A joint experimental–simulative approach quantitatively determines the interface defect density to be more than one order in magnitude larger for the n–i–p architecture. Among the polymeric hole transport layers investigated for n–i–p devices, poly(3-hexylthiophen-2,5-diyl) (P3HT) exhibits the most favorable energy-level alignment to Pb/Sn perovskites. These results clarify the nature of V_{OC} losses in Pb/Sn perovskites and highlight the necessity to develop electron extraction layers with a significantly reduced interface defect density.


1. Introduction

Organic–inorganic hybrid perovskites have attracted immense attention, owing to their great optoelectronic properties used in various electronic devices. The power conversion efficiency

(PCE) of single-junction perovskite solar cells (PSCs) has progressed rapidly from 3.8%^[1] to 25.5%.^[2] The device efficiency can be further improved by combining narrow- and wide-bandgap perovskites into a tandem configuration, which can effectively reduce the inherent losses related to thermalization and subbandgap transmission.^[3] Compared to hybrid tandem solar cells based on Si or CIGS subcells, all-perovskite tandem solar cells can be manufactured with the same printing methods. In order to keep the investment costs in a production line as low as possible, it is imperative to design the production process with the smallest possible number of process technologies, which should also have a comparable production speed and throughput. Printing technologies meet these requirements to a very high degree and are therefore regarded to enable the lowest costs for a future perovskite single-junction and tandem junction module technology.^[4,5]

It has been reported that the current record PCEs of 2-terminal and 4-terminal all-perovskite tandem solar cells have reached 25.6%^[6] and 21.0%,^[7] respectively. Mixed lead (Pb)–Tin (Sn) perovskites are perfect candidates for the narrow-bandgap subcell in the tandem configuration because of their tunable bandgap (E_g) of around 1.2 eV together with competitive device efficiencies of above 20.0%.^[8–11] However, the partial replacement

K. Zhang, K. Forberich, L. Lüer, J. G. Cerrillo, W. Meng, X. Du, V. M. Le Corre, Y. Zhao, N. Li, C. J. Brabec
Institute of Materials for Electronics and Energy Technology (i-MEET)
Department of Materials Science and Engineering
Friedrich-Alexander-Universität Erlangen-Nürnberg
Martensstrasse 7, Erlangen 91058, Germany
E-mail: ning.li@fau.de; christoph.brabec@fau.de

 The ORCID identification number(s) for the author(s) of this article can be found under <https://doi.org/10.1002/aesr.202100156>.

© 2021 The Authors. Advanced Energy and Sustainability Research published by Wiley-VCH GmbH. This is an open access article under the terms of the Creative Commons Attribution License, which permits use, distribution and reproduction in any medium, provided the original work is properly cited.

DOI: 10.1002/aesr.202100156

K. Forberich, L. Lüer, X. Du, Y. Zhao, N. Li, C. J. Brabec
Helmholtz-Institute Erlangen-Nürnberg for Renewable Energy (HI ERN)
Immerwahrstrasse 2, Erlangen 91058, Germany

T. Niu, Q. Xue
State Key Laboratory of Luminescent Materials and Devices, Institute of Polymer Optoelectronic Materials and Devices, School of Materials Science and Engineering
South China University of Technology
381 Wushan Road, Guangzhou 510640, P. R. China

L. J. A. Koster
Zernike Institute for Advanced Materials
University of Groningen
Nijenborgh 4, 9747 AG Groningen, The Netherlands

of Pb with Sn in the mixed Pb/Sn perovskites significantly alters the crystal growth process. In addition, the mixed Pb/Sn perovskites suffer from p-type self-doping as the unstable Sn^{2+} turns into Sn^{4+} in the bulk or at the surface, resulting in an undesirable efficiency deficit of PSCs.^[12] Many strategies have been proposed to fabricate high-quality perovskite films with suppressed formation of stannic species, for instance, by adding tin fluoride (SnF_2),^[13] thiocyanate,^[14] guanidine-based compounds,^[15] Sn powder^[16,17] and zwitterionic molecules^[6] into perovskite precursors.

However, the performance of PSCs is strongly influenced by the nature and properties of interfacial layers, which are imperative for achieving high-quality Pb/Sn mixed perovskites with desired optoelectronic properties and stability.^[18,19] PSCs are generally classified by device polarity as either p-i-n or n-i-p device structures. **Figure 1b** and Table S1, Supporting Information, summarize the development of mixed Pb/Sn PSCs. The efficiency of Pb/Sn mixed PSCs in the p-i-n configuration so far achieved the highest PCE of 21.7%,^[6] while the development of PSCs in the n-i-p architecture lacked behind. Considering the great performances of wide-bandgap subcell were achieved by n-i-p structure and the alignment of device architectures between subcells,^[20] further improvement of efficiency and understanding of energy losses in n-i-p-based narrow-bandgap subcells are quite important to approach the

theoretical efficiency limit of all perovskite-based tandem solar cells. Compared with p-i-n devices, the limitation of n-i-p devices was mainly due to their larger ($E_g - V_{\text{OC}}$) loss of typically more than 0.5 V (Figure 1c) and their lower fill factors (FFs) (Figure 1d) of typically below 0.7. Exchanging the upper and lower interfaces of PSCs obviously causes a significant variation in device performance. On the one hand, the underlying interlayer plays an important role in the crystallization process of perovskite layers; on the other hand, the upper interlayer is responsible for passivating surface defects and protecting the absorber layer from detrimental environmental factors. Metal oxides are the commonly used n-type semiconductors in the conventional structure. Hayase et al. reported the first conventional low-bandgap PSCs based on titanium dioxide (TiO_2) with a PCE of 4.18%.^[21] They found that chemical reactions between the defects on TiO_2 and SnI_2 can create interfacial traps and thus hinder electron extraction.^[22] The performance of mixed Pb-Sn perovskites was recently improved to 15.5% by Yuan et al. by using chloride-modified TiO_2 and top surface passivation with 2D ligands.^[23] Snaith et al. reported the fabrication of low-bandgap perovskite cells using low temperature processed tin dioxide (SnO_2) modified with phenyl- C_{61} -butyric acid methyl ester (PCBM).^[24] Yip et al. reported the modification of SnO_2 with zinc oxide and C_{60} self-assembled monolayer (C_{60} -SAM)

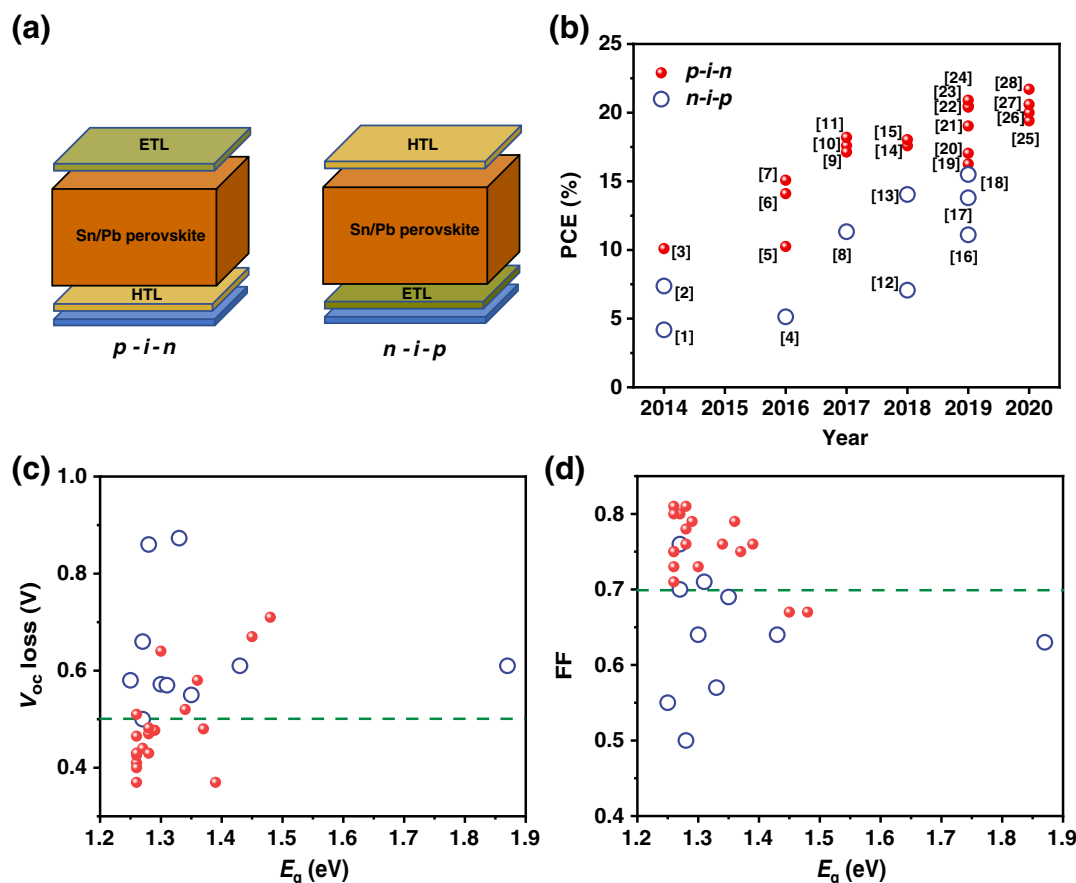


Figure 1. a) The device configuration of Pb/Sn mixed PSCs and b) the corresponding development of PCE. c) V_{OC} loss ($E_g - V_{\text{OC}}$) and d) FF corresponding to bandgap (E_g) in the literature (details can be found in Table S1, Supporting Information). The green dashed lines in (c) and (d) represent the ($E_g - V_{\text{OC}}$) loss of 0.5 V and FF of 0.7, respectively.

in order to reduce energy-level mismatch at the bottom interface, leading to suppressed interfacial recombination losses and increased V_{OC} .^[25] In all these cases, the passivation of the metal oxide layer, which was frequently demonstrated with an organic n-type semiconductor like PCBM, was crucial for the growth of qualitative low-bandgap perovskites.

As for the p-type interface, 2,2',7,7'-tetrakis-(*N,N*-di-4-methoxyphenylamino)-9,9'-spirobifluorene (spiro-MeOTAD) was the most frequently used hole transport material in the n-i-p structure.^[26–29] However, the Pb/Sn perovskites are subject to degradation or decomposition induced by the dopants (Li or Co salts) which, on the other hand, are inevitable to obtain favorable hole transport properties. This issue was partly resolved by applying a dicationic salt of spiro-OMeTAD, spiro (TFSI)₂,^[24,30] or by inserting an interlayer prior to the deposition of spiro-OMeTAD (i.e., poly(4-vinylpyridine)^[31] or phenylethylammonium iodide^[23]). Owing to the diversity and promising conductivity, conductive polymers, such as poly[4,4'-bis(2-butyloctyloxy-carbonyl-[2,2'-bithiophene]-5,5-diyl)-alt-(2,2'-bithiophene-5,5'-diyl)] (PDCBT),^[32] poly(3-hexylthiophen-2,5-diyl) (P3HT),^[33] poly(triaryl amine) (PTAA), and poly(4-butylphenyldiphenylamine) (PolyTPD),^[34] are promising hole transport layers (HTLs) for fabricating PSCs with competitive efficiency and stability. In particular, P3HT was reported to achieve good energy alignment with the valence band maximum (VBM) of Pb/Sn perovskites.^[21] However, the fast oxidation of Pb/Sn perovskite films when exposed to air makes it very difficult to develop a reliable understanding of the fundamental processes at the anode interface for the n-i-p-type PSCs. The discrepancies documented in the literature suggest that the influence of interface layers on the underlying loss mechanisms has to be studied more quantitatively.

Herein, we perform a detailed study on the origin of the relatively low efficiency of the n-i-p low-bandgap PSCs and investigate the functionality of commonly used polymeric HTLs, including PolyTPD, PTAA, P3HT, and PDCBT. In order to exclude the influence of the underlying cathode interface, the mixed Pb/Sn perovskite layer is deposited on a thermally evaporated fullerene (C₆₀) substrate. We find that only P3HT and PTAA can effectively extract holes from the low-bandgap perovskite layer, while PolyTPD and PDCBT block the hole extraction due to their relatively deep highest occupied molecular orbital (HOMO) levels. By calculating the quasi-Fermi level splitting (QFLS) of different perovskite/interlayer junctions and simulating the *J*-*V* curves of devices, it is found that the nonradiative V_{OC} loss in Pb/Sn SCs is dominated by the electron transport layer (ETL)/perovskite interface, while the HTL/perovskite interface shows a reduced interface defect density. The findings of this work highlight the importance of developing novel n-type as well as p-type interface materials offering a low interface defect density in parallel to well-aligned energy levels in order to develop highly efficient and stable narrow-bandgap PSCs.

2. Results and Discussions

2.1. Morphology and Crystallization of Perovskite Films on Different Substrates

The properties of substrate layers are responsible for the crystallization of perovskite film, charge selectivity, and surface

passivation. PEDOT:PSS has been universally used to fabricate Sn-based PSCs in a p-i-n configuration owing to its excellent wetting property and favorable energy levels, while for the n-i-p type devices the perovskite was typically deposited on a metal oxide layer. The fullerene materials (PCBM and C₆₀) were widely used as ETL in perovskite devices because of their good electron extraction and surface passivation properties.^[35–38] To get a better understanding of the underneath interlayer impacts, metal oxides (ZnO and SnO₂), fullerene (PCBM and C₆₀) as well as PEDOT:PSS films have been processed in the current work. Scanning electron microscopy (SEM) images of perovskite films grown on n-type substrates (ZnO, SnO₂, PCBM, and C₆₀) are shown in Figure S1, Supporting Information. The results showed that the quality of the top surface of perovskite films grown on metal oxides or PCBM was rather poor, reflected by the presence of lots of pin-holes and small-sized crystals. However, as shown in Figure 2a–f, the morphology of perovskite films deposited on glass, C₆₀, and PEDOT:PSS demonstrated that these substrates were conducive to form compact and large-grained nanocrystal films (average grain size was 450 nm), which is favorable to suppress leakage currents and expected to reduce nonradiative recombination in the device, respectively.

Figure 2g shows the X-ray diffraction (XRD) patterns of perovskite films on glass, C₆₀, and PEDOT:PSS. The Bragg reflections in Pb/Sn perovskite films are consistent with powder crystals that are crystalline in the cubic *Pm* $\bar{3}$ *m* space group, where the peaks positioning at 14.1°, 20.0°, 24.5°, 28.3°, 31.7°, 34.9°, 40.5°, and 43.1° were indexed to the reflections of (100), (110), (111), (200), (210), (211), (220), and (300).^[39,40] The intensities of two main reflection peaks (100) and (200) of perovskite films on C₆₀ were higher than those on either other n-type interlayers (Figure S2a, Supporting Information) or PEDOT:PSS, indicating enhanced crystallinity for perovskites grown on C₆₀. Additionally, the strain in lattices throughout perovskite films on different substrates was evaluated by Williamson–Hall plots. The details of strain calculation are given in Figure 2h and Figure S2b–2e, Supporting Information. Interestingly, the slope calculated for perovskite on glass and C₆₀ was the highest among the films, indicating that these perovskite layers are subject to the largest strain. Nevertheless, in our case the interlayer exhibited only a slight impact on strain formation, which probably is more expressed for other compositions, such as cesium and bromide containing ones.

2.2. Device Performances of n-i-p and p-i-n Devices

Compared with Pb-based perovskite, the Sn-containing perovskites are prone to redox reactions, which result in the formation of 2D phases (A₂SnI₆) or tin dioxide.^[41] Figure S3a, Supporting Information, shows the Sn 3*d* X-ray photoelectron spectra (XPS) of the mixed Pb/Sn perovskite film, indicating the existence of a Sn⁴⁺ signal (484.75 and 493.20 eV). As shown in Figure S3b, Supporting Information, the XPS peaks of Sn 3*d*_{5/2} shifted from 484.25 to 483.90 eV and Sn 3*d*_{3/2} shifted from 492.65 to 492.35 eV after etching to different depths. A thin top layer of Sn⁴⁺ species formed at the surface of perovskite film indicated the facile oxidation happened. And the formation of such a

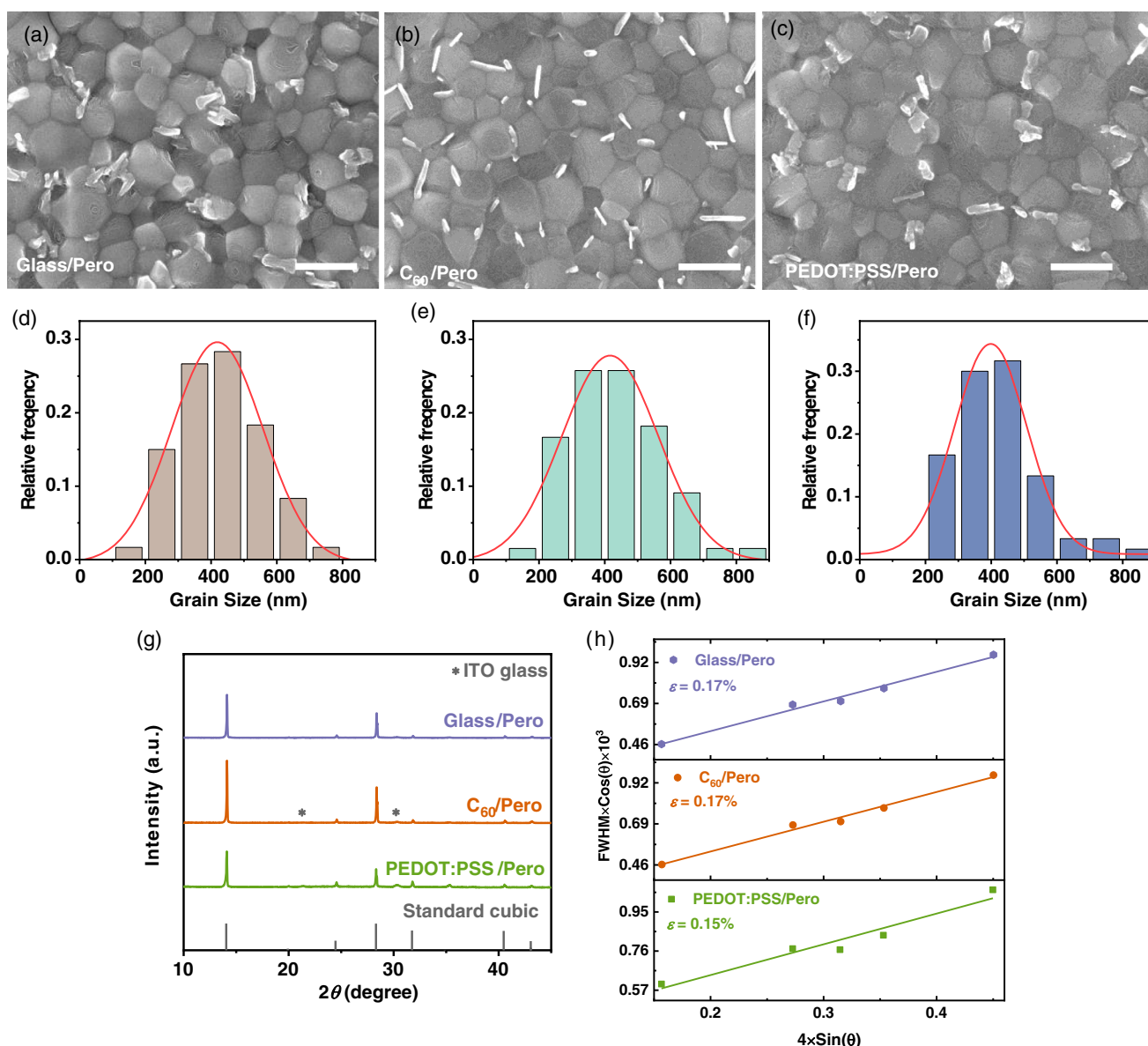


Figure 2. Morphology of perovskite films deposited on a) glass, b) C_{60} , and c) PEDOT:PSS; the scale bars are 1 μm ; and d–f) corresponding grain size distributions. g) XRD patterns (the peaks with an asterisk are related to ITO glass) and h) Williamson–Hall plots of perovskite films. The standard cubic powder XRD pattern was from Ke et al.^[40]

surface state during processing or measurement makes it challenging to experimentally determine the real properties of either valence band maximum (VBM) or conduction band minimum (CBM) (e.g., XPS or ultraviolet photoelectron spectroscopy [UPS]). The energy levels of perovskite consisting of $(\text{MAPbI}_3)_{0.4}(\text{FASnI}_3)_{0.6}$ determined by UPS were reported with a large deviation between measurements in the literature^[17,23,42,43] (as shown in Table S2, Supporting Information). As such, the energetics of the perovskite interface is yet not fully resolved for the mixed Pb/Sn perovskites. This complicates to provide guidance on the rational selection or optimization of interlayers in terms of defect-assisted nonradiative recombination, energy-level alignment, and parasitic series resistance.

Consequently, we investigated the influence of interlayers in the n–i–p device configuration by selecting four ETLs and four HTLs to fabricate PSCs (Figure 3a). Initially, devices based on different ETLs (ZnO , SnO_2 , PCBM, and C_{60}) and the same HTL (P3HT) were studied. The J – V curves of champion devices are displayed in Figure S4, Supporting Information, and the corresponding average photovoltaic parameters are listed in Table S3, Supporting Information. The devices based on either metal oxide films or PCBM as ETL showed inferior performance when compared with C_{60} -based PSCs, which yielded a V_{OC} of 0.58 V, a short-circuit current density (J_{SC}) of 27.62 mA cm^{-2} , and a FF of 65.7% resulting in a PCE of 10.5%. As shown in Figure S5, Supporting Information, other most widely used

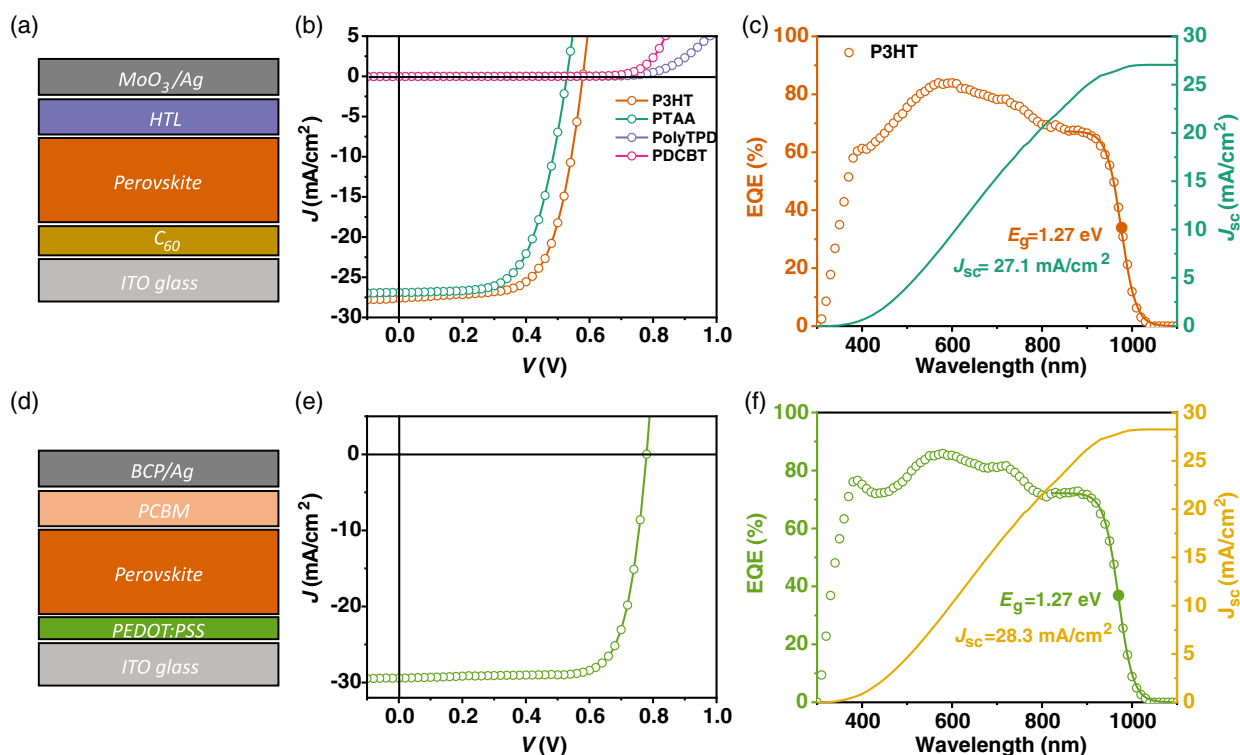


Figure 3. Device configurations of: a) n-i-p and d) p-i-n PSCs. The J - V curves of b) n-i-p devices with different polymeric HTLs and e) p-i-n device. EQE spectra of c) n-i-p devices based on P3HT and f) p-i-n-based PSCs.

n-i-p device structures, such as ITO/TiO₂/Pero/Spiro-OMeTAD/Au, ITO/TiO₂/Pero/P3HT/MoO₃/Ag, and ITO/SnO₂/PCBM/Pero/P3HT/MoO₃/Ag, have also been investigated, but these devices also exhibited severe losses in V_{OC} , J_{SC} , and FF. The large V_{OC} and FF deficits in metal oxide-based devices indicated significant carrier recombination at the ETL/perovskite interface, which is consistent with the conclusions from the literature.^[22] Besides, the PCBM layer is subject to dissolving in solvents (DMF/DMSO) during the annealing process, resulting in an unfavorable contact between indium tin oxide (ITO) and the perovskite film. Among these ETLs, C₆₀ was found to be a decent interlayer to efficiently extract electrons and, therefore, was utilized to prepare n-i-p devices for further investigations.

In the following, four organic polymers with different HOMO levels were selected as the HTLs to construct the n-i-p PSCs: PolyTPD, PDCBT, PTAA, and P3HT. Figure 3b shows the J - V curves of PSCs with different polymeric HTLs, and the corresponding photovoltaic characteristics are listed in Table 1. Aside from the device based on P3HT, PTAA-based champion device yielded a V_{OC} of 0.53 V, a J_{SC} of 26.9 mA cm⁻², and a FF of 62.7% resulting in a PCE of 8.9%. However, the devices based on PDCBT and PolyTPD exhibited significantly lower J_{SC} and FF. The S-shaped J - V curves suggest a significant energetic barrier at the perovskite/HTL interface which blocks hole extraction from these two polymers and it will be further discussed in the following sections. This will be discussed in more detail in the following section. The external quantum efficiency

Table 1. The J - V photovoltaic characteristics of the best devices (average parameters) with n-i-p and p-i-n configurations.

HTL	V_{OC} [V] best [avg.] ^{a)}	J_{SC} [mA cm ⁻²] best [avg.] ^{a)}	FF [%] best [avg.] ^{a)}	PCE [%] best [avg.] ^{a)}	V_{OC} loss [V] [$E_g - V_{OC}$]/ q
ITO/C ₆₀ /Perovskite/HTL/MoO ₃ /Ag					
P3HT	0.58 (0.57)	27.62 (27.60)	65.7 (64.4)	10.5 (10.2)	0.69
PTAA	0.53 (0.52)	26.90 (27.48)	62.7 (61.5)	8.9 (8.8)	0.74
PolyTPD	0.55 (0.56)	0.59 (0.29)	20.3 (20.5)	0.1 (0.03)	0.72
PDCBT	0.56 (0.53)	0.27 (0.04)	34.0 (21.3)	0.1 (0.0)	0.71
ITO/PEDOT:PSS/Perovskite/PCBM/BCP/Ag					
PEDOT:PSS	0.78 (0.77)	29.42 (28.93)	76.6 (74.2)	17.6 (16.6)	0.49

^{a)}The values were determined from the average of individual 12 solar cells.

(EQE) of P3HT-based device is exhibited in Figure 3c, accompanied by the integrated J_{SC} . The integrated J_{SC} of 27.1 mA cm^{-2} is comparable to the value extracted from the J - V characteristics. In addition, the bandgap (E_g) was determined with 1.27 eV by fitting the inflection point of the EQE spectra assuming a sigmoid function.^[44]

To get a comparison between different device configurations, devices with p-i-n structure (Figure 3d) were fabricated. The J - V curve of the champion solar cell is displayed in Figure 3e and the corresponding photovoltaic characteristics are summarized in Table 1. The device exhibited a PCE of 17.6% along with a V_{OC} of 0.78 V, a J_{SC} of 29.42 mA cm^{-2} , and a FF of 76.6%. An integrated J_{SC} of 28.3 mA cm^{-2} was calculated from the EQE spectrum in Figure 3f and the estimated E_g (1.27 eV) was identical to the n-i-p device. The V_{OC} losses of the devices in the n-i-p and p-i-n structure are summarized in Table 1. As it is, most of the n-i-p devices exhibited a significantly larger V_{OC} loss (above 0.70 V) as compared to that of p-i-n devices (0.49 V), indicating that more pronounced charge recombination in the bulk or at the interface between perovskite and interlayers is taking place for n-i-p PSCs.

2.3. QFLS in Perovskite/Interlayer Junctions

In order to shed light on the mechanism taking place in Pb/Sn PSCs with large energy losses, a detailed analysis was carried out to quantify the respective contributions. The determination of QFLS of perovskite film, perovskite/interlayer junctions, and complete devices by measuring the absolute photoluminescence (PL) is an effective approach to quantitatively calculate the energy losses. Based on the assumption that all PL emission is coming

from the radiative recombination of free carriers in perovskite film, the PL quantum yield (PLQY) efficiency has the relationship to the QFLS (as shown in Equation (1)) according to radiative recombination current density that governed by the efficiency limit.^[34,45,46]

$$\begin{aligned} \text{QFLS} &= \text{QFLS}_{\text{rad}} + kT \ln(\text{PLQY}) \\ &= kT \ln\left(\frac{J_G}{J_{0,\text{rad}}}\right) + kT \ln\left(\frac{J_{\text{rad}}}{J_{\text{rad}} + J_{\text{non-rad}}}\right) \end{aligned} \quad (1)$$

where QFLS_{rad} is the quasi-Fermi level splitting for the perovskite layer with radiative recombination at the thermodynamic limit of V_{OC} which is obtained for a device with energetically perfectly aligned interfaces. k is the Boltzmann constant and the solar cell is under thermal equilibrium at $T = 300 \text{ K}$. QFLS_{rad} can be further calculated by the ratio of generation current density J_G and the dark radiative saturation current density $J_{0,\text{rad}}$ that can be determined by the integrating $\text{EQE}_{\text{PV}}(E)$ spectrum (Equation (2)) times the background black body radiation spectrum $\phi_{\text{bb}}(E)$ (Equation (3)) according to the detailed balance principle.^[45,47]

$$J_{0,\text{rad}} = q \int \text{EQE}_{\text{PV}}(E) \phi_{\text{bb}}(E) dE \quad (2)$$

$$\phi_{\text{bb}}(E) = \frac{2\pi E^2}{(h^3 c^2)} \exp\left(-\frac{E}{kT}\right) \quad (3)$$

where q is the elementary charge, E the photo energy, h the Planck constant, and c the light velocity in vacuum. Figure 4a,d shows the photovoltaic quantum efficiency of n-i-p and

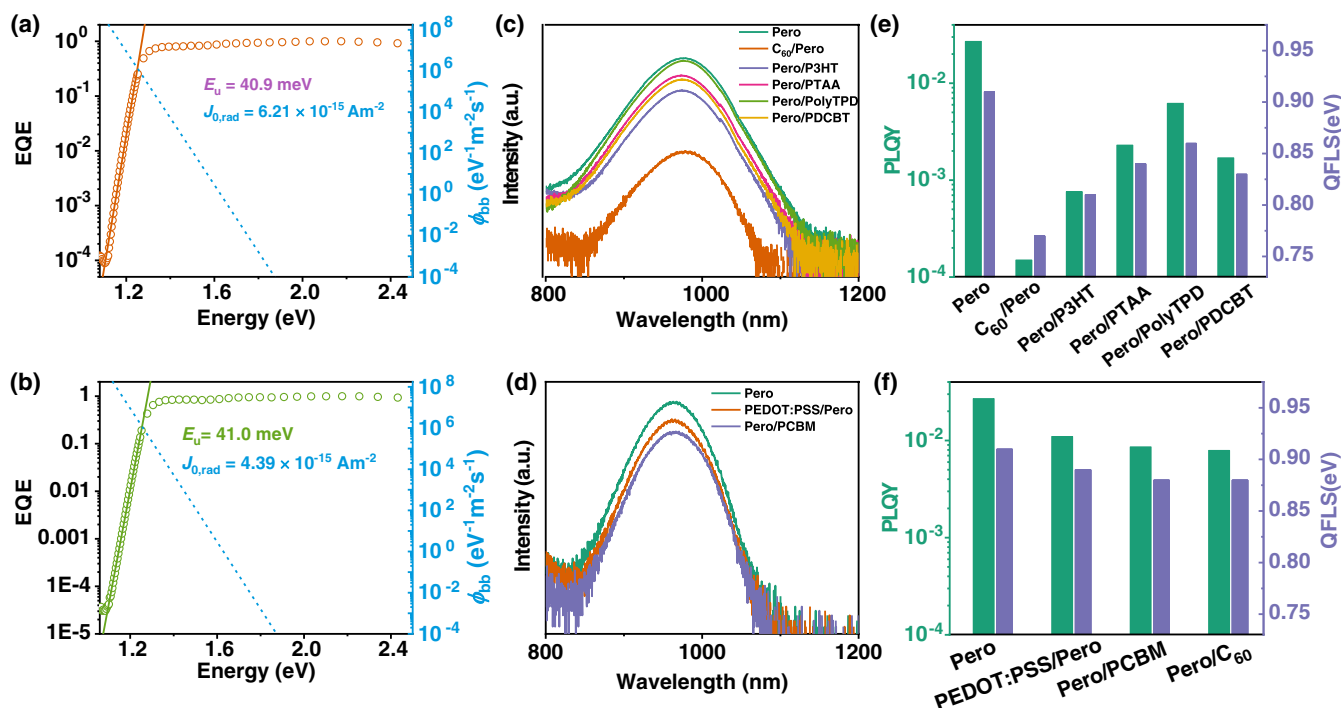


Figure 4. EQE spectra of a) n-i-p device based on P3HT and b) p-i-n device. PL spectra of perovskite/interlayer junction in c) n-i-p and d) p-i-n configurations. The calculated PLQY and QFLS of the samples in e) n-i-p and f) p-i-n configurations.

p-i-n devices on a logarithmic scale, respectively. The $EQE_{PV}(E)$ spectra were measured by the Fourier transform photocurrent spectroscopy (FTPS) over several orders in magnitude. The Urbach energy (E_u) related to electronic disorder in the continuum of states can be obtained by fitting the absorption tail via the relationship of $\alpha = \alpha_0 \exp(E - E_0/E_u)$. The fitted Urbach energies of n-i-p and p-i-n devices were determined to be ≈ 41.0 meV which is larger than the values of c-Si (12.0 meV),^[48] GaAs (7.5 meV),^[49] CIGS (31.0 meV),^[50] or MAPbI₃ (14.0 meV).^[51] The large E_u is explained by self-doping behavior of Pb/Sn perovskites which induces a large trap density resulting in severe energy losses if E_u exceeds the thermal energy kT (25.7 meV).^[52,53] The $J_{0,rad}$ of the devices based on n-i-p and p-i-n was estimated to be 6.21×10^{-15} and 4.39×10^{-15} A m⁻², respectively. The QFLS_{rad} of both kind of devices was determined to be 1.0 eV.

The PLQY of perovskite films is quite sensitive to specific conditions, such as illumination intensity, light soaking effect, outcoupling, or degradation. To exclude the influence of degradation by the atmosphere, all samples were encapsulated with a covering glass and the edges were sealed with glue in a nitrogen-filled glove box. Figure S6a,b, Supporting Information, shows the PLQY of glass/perovskite films stored in the glove box over time and the results indicated that films remained stable within the 2 days of measurement period. As shown in Figure S6c-f, Supporting Information, the Pb/Sn perovskite film exhibited a decreased PLQY after 1 min exposure under 405 nm laser light equivalent to 1 sun illumination, which was contrastingly different to the light-soaking effect of Pb-based perovskite for which we observed an increase of PLQY. Thus, the PL measurements were carried out with the same time exposure. The PLQY excited from the bottom and top sides of perovskite film was studied (Figure S7a,b, Supporting Information). We found that the nonradiative recombination at the top side is comparable with the one at the bottom side. The dependence of PLQY on the illumination of laser intensities is shown in Figure S7c,d, Supporting Information; the results showed that PLQY decreased with lowering illumination intensities to below 1 sun, but it became constant with higher photon flux, indicating the saturation of trap-filling.

Figure 4c,d illustrates the PL spectra of perovskite/interlayer junctions and the PL spectra measured with integrated sphere are shown in Figure S8a,b, Supporting Information. The calculated PLQY and QFLS according to Equation (1) are plotted in Figure 4e,f and the corresponding parameters are summarized in Table 2. The PLQY of glass/perovskite sample was 2.7×10^{-2} under the illumination of 1 sun and such a high value is reasonable in Pb/Sn-based perovskites because of their fast radiative recombination rate due to self p-type doping.^[54] The QFLS of pure perovskite film was 0.91 eV, which is only 90 meV smaller than the QFLS in the radiative limit. Among the perovskite/interlayer junctions in the n-i-p configuration, the C₆₀/perovskite exhibited the lowest PLQY, resulting in a significant QFLS loss of 230 meV. This large loss should contribute from high interface trap density formed during processing and that could be related to the unfavorable hydrophobicity of C₆₀ substrate. We note that the properties of underneath substrate could influence the morphology or crystallization of perovskite film (as shown in Figure 2), but these features cannot explain the bulk nonradiative

Table 2. The PLQY and QFLS values of perovskite film and perovskite/interlayer junctions.

Junctions	PLQY	QFLS [eV]	Nonradiative loss [eV]
Glass/Pero	2.7×10^{-2}	0.91	0.09
n-i-p configuration	—	—	—
Glass/C ₆₀ /Pero	1.5×10^{-4}	0.77	0.23
Glass/Pero/P3HT	7.6×10^{-4}	0.81	0.19
Glass/Pero/PTAA	2.3×10^{-3}	0.84	0.16
Glass/Pero/PolyTPD	6.2×10^{-3}	0.86	0.14
Glass/Pero/PDCBT	1.7×10^{-3}	0.83	0.17
p-i-n configuration	—	—	—
Glass/PEDOT:PSS/Pero	1.1×10^{-2}	0.89	0.11
Glass/Pero/C ₆₀	7.9×10^{-3}	0.88	0.12
Glass/Pero/PCBM	8.6×10^{-3}	0.88	0.12

recombination losses, which could be more related to the density of subgap states of perovskite films. By comparing different perovskite/HTL junctions, the interface between polyTPD and perovskite was superior to the interfaces formed by other polymers reflecting that perfect energy-level alignment can reduce otherwise significant extraction-induced V_{OC} losses. On the other hand, the QFLS values of PEDOT:PSS/perovskite and perovskite/PCBM or C₆₀ junctions are 0.89 and 0.88 eV, respectively. The results reveal that the perovskite/ETL interface dominated the QFLS loss in either n-i-p or p-i-n PSCs.

2.4. Electrical Properties of n-i-p Devices and Nonradiative Losses at V_{OC}

The QFLS of perovskite/interlayer junction provides a crucial guidance under open-circuit condition to select interlayers toward less photovoltage deficit. However, the device performance is also related to carrier transport properties in the bulk or at the interfaces. The QFLS of perovskite/PolyTPD was decent but the device suffered from low performance, which resulted from a barrier for hole extraction. Because of the exponential relationship between the current and energy barrier, the measured current is very sensitive to the barrier height.^[55] As shown in Figure 5a, the hole extraction from perovskite to HTLs is related to positive bias and hole injection from HTL to perovskite under reverse bias. The hole current extracted by PolyTPD and PDCBT was significantly lower, which can be attributed to their deeper HOMO levels with respect to the VBM of perovskite, forming an extraction barrier at the interface, while the hole extraction from perovskite to P3HT or PTAA was more efficient. Additionally, the Mott-Schottky (M-S) plots of the devices with different HTLs were measured and the results are shown in Figure 5b. The built-in voltage (V_{bi}), doping density (N), and depletion region width (w) can be extracted from the M-S plots at forward bias based on the one-side abrupt p-n junction model.^[56] The charge density profile in devices strongly depends on the relative doping density, thus different models and the density of state for perovskite were reported by two orders of magnitude lower than that of transporting layers. Therefore,

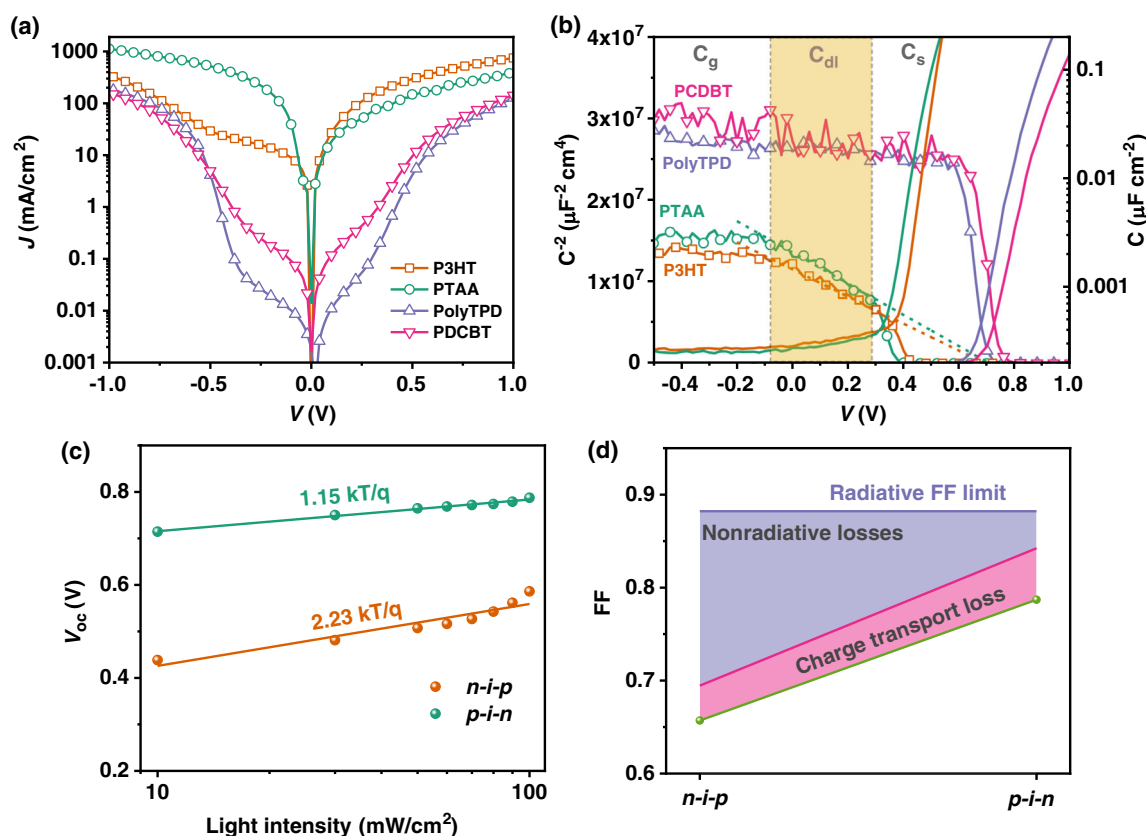


Figure 5. a) The J - V curves of hole-only devices with different HTLs, the configuration was ITO glass/PEDOT:PSS/perovskite/HTLs/MoO₃/Ag. b) M-S plots of the device based on n-i-p configuration. c) V_{OC} versus light intensity of the n-i-p device based on P3HT and p-i-n device and d) contributions of FF losses mechanisms for n-i-p and p-i-n devices.

the one-side abrupt p-n junction model with the assumption that the defect density in a layer exceeds the defect density in the adjacent layer was adapted.^[57] The relationship between capacitance and bias is given by the following equation

$$C_{dl}^{-2} = \frac{2(V_{bi} - V)}{q\epsilon\epsilon_0 N} \quad (4)$$

where q is the elementary charge, ϵ is the dielectric constant of perovskite, ϵ_0 is the vacuum permittivity, and V is the applied bias. Based on the requirement of charge neutrality within the space charge region, the depletion layer width w can be calculated by

$$w^2 = \frac{2\epsilon\epsilon_0(V_{bi} - V)}{qN} \quad (5)$$

The devices based on P3HT and PTAA showed three distinct regions, namely, geometrical capacitance (C_g), depletion layer capacitance (C_{dl}), and electrode polarization/charge accumulation induced capacitance (C_s), while only C_g and C_s were distinguishable for the devices based on PolyTPD and PDCBT. The absence of C_{dl} also implied that there was no internal charge field in the latter two devices. As listed in Table 3, the V_{bi} of 0.69 and 0.71 V was determined from the intercept with x-axis by linearly fitting for the devices based on P3HT and PTAA, respectively.

Table 3. Calculated built-in potential, doping density, and depletion width for n-i-p device based on P3HT and PTAA.

Device	V_{bi} [V]	N [cm ⁻³]	w [nm]
P3HT	0.69	2.65×10^{16}	283.0
PTAA	0.71	2.36×10^{16}	263.4

The doping density of 2.65×10^{16} cm⁻³ for P3HT and 2.36×10^{16} cm⁻³ for PTAA was calculated from the slope and the depletion region width of 283.0 nm for P3HT and 263.4 nm for PTAA was yielded at zero bias.

To investigate the contributions from charge transport and nonradiative recombination in energy losses of n-i-p and p-i-n devices, the V_{OC} versus light intensities have been carried out. According to SQ model, the relationship between FF_0 and V_{OC} can be related by the following approximation equation^[58]

$$FF_0 = \frac{\frac{qV_{OC}}{nkT} - \ln\left(\frac{qV_{OC}}{nkT} + 0.72\right)}{\frac{qV_{OC}}{nkT} + 1} \quad (6)$$

where FF_0 is the fill factor without resistive losses and n is ideal factor. Figure 5c shows the V_{OC} measured under different light intensities and the ideal factors (n) were obtained based on the

relationship between V_{OC} and light intensity I , $qV_{OC} = E_g - nkT \ln(I_0/I)$. The n-i-p device exhibited an ideal factor of 2.23, which was higher than 1.15 of p-i-n device. Combining with formula (6), the contributions of FF losses in solar cells were calculated and shown in Figure 5d. The results indicated that charge transport was not the main reason for FF loss in n-i-p devices, whose inferior FF was primarily contributed from severe trap-assisted nonradiative recombination from when compared with p-i-n devices.

2.5. Drift-Diffusion Simulation of $J-V$ Curves

To further clarify the losses in different devices, 1D drift-diffusion (DD) simulation of $J-V$ curves was carried out with the SIMsalabim simulator developed by Koster et al.^[59–61] (the SIMsalabim can be accessed from Github: <https://github.com/kostergroup/SIMSsalabim>). The simulations were based on the documented and experimental data for perovskite devices and Table S4, Supporting Information, lists the input parameters for DD simulations. The key properties, i.e., energy levels and surface trap densities, relative to interfaces were chosen as fit parameters to get good agreement with the experimental $J-V$ curves. The simulated $J-V$ curves of n-i-p PSCs with different HTLs are shown in Figure S9, Supporting Information. The simulated results confirm that the origin of the poor performance of

PolyTPD- or PDCBT-based devices stemmed from a too large energy level offset, which was determined to be about 0.4 eV or more. On the other hand, compared with P3HT-based PSCs, the surface defect density for the PTAA-based device was low. However, the lower hole mobility of the PTAA layer and a small extraction barrier at the perovskite/PTAA interface resulted in a reduced V_{OC} and FF for PTAA-based PSCs.

Figure 6a shows the experimental and simulated $J-V$ curves for both n-i-p and p-i-n devices. The trap density extracted from the simulation at the perovskite/ C_{60} and the perovskite/P3HT interfaces is 4.0×10^{13} and $7.5 \times 10^{12} \text{ m}^{-2}$, respectively. While in the p-i-n device, the trap densities are determined to be $1.5 \times 10^{12} \text{ m}^{-2}$ at the perovskite/PEDOT:PSS interface and $4.5 \times 10^{12} \text{ m}^{-2}$ at the perovskite/PCBM interface. It can be concluded that the lower device performance of n-i-p devices is caused by enhanced interface recombination as compared to p-i-n devices. Nevertheless, the higher trap density at the perovskite/ETL interface in either n-i-p or p-i-n structure reveals that this interface is causing the dominant losses in Pb/Sn PSCs by today, as illustrated in Figure 6b. In order to identify the direction toward reducing energy losses in Sn/Pb PSCs, we carried out further simulations to investigate the impact of defect density and energetic alignment at the perovskite/ETL interface based on the $J-V$ characteristic of a p-i-n device. Lowering the trap density at the interface can contribute to enhanced V_{OC} (Figure 6c), which is related to low nonradiative recombination

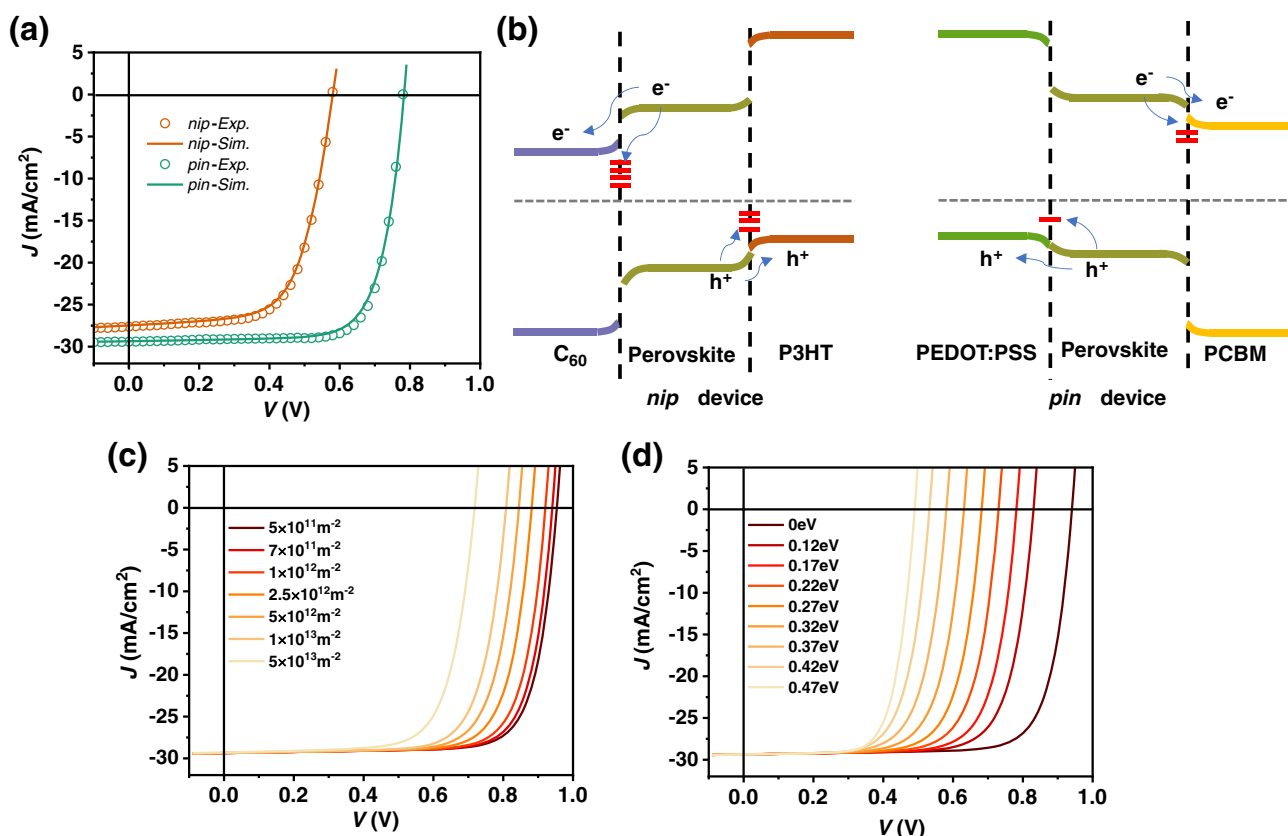


Figure 6. a) Experimental and simulated $J-V$ curves and b) energy band structure of p-i-n and n-i-p devices. The impact of c) interfacial trap density (CBM of ETL layer was set to be aligned with the VBM of perovskite) and d) energy-level offset (surface traps was $7 \times 10^{11} \text{ m}^{-2}$) at perovskite/ETL interface.

and hence high QFLS. The energy-level offset (Figure 6d) also exhibits a significant influence on the energy losses, and a larger energy level offset induces a serious V_{OC} drop.

3. Conclusion

In this work, we demonstrated the importance of n- and p-type interface engineering in Pb/Sn mixed PSCs by quantitatively determining the specific interface deficiencies in terms of V_{OC} losses. C_{60} is a promising n-type contact, which can afford perovskite films with high quality. Compared to the typical metal oxide interfaces, C_{60} does suppress surface defects. For the p-type interface, it was found that P3HT is a good candidate with the lowest energy barrier at the hole extraction interface compared to other conducting polymers (i.e., PTAA, PolyTPD, and PDCBT). Moreover, the PLQY and $J-V$ curve simulation indicated that the energy losses in the mixed Pb/Sn PSCs were dominated by nonradiative recombination at the perovskite/ETL interface. This work demonstrates the importance of interface engineering and control over crystal growth for Pb/Sn PSCs and sheds light on the energetic alignment and nonradiative recombination between perovskite and charge selective layers for further development of low bandgap PSCs.

4. Experimental Section

Materials: The ITO glass substrates were purchased from CSG Holding Co., Ltd. SnO_2 nanoparticle (2.5 wt% in IPA) was obtained from Alfa Aesar. ZnO nanoparticles (N10) and MoO_3 powders were provided by Avantama. PCBM and C_{60} powders (99.95%) were bought from Nano-C. MAI and FAI (>99.99%) were ordered from Greatcell Solar Ltd. PbI_2 powders (99.99%) were obtained from TCI Co., Ltd. SnI_2 (99.99%), SnF_2 (99.0%), and $Pb(SCN)_2$ (99.5%) were purchased from Sigma-Aldrich. All the polymeric hole transport materials used were obtained from Merck and used as received. All the solvents mentioned were received from Sigma-Aldrich.

Device Fabrication: Devices were prepared on ITO-coated glass. All the substrates for the deposition of perovskite films were ultrasonically cleaned in succession with acetone and isopropanol, with which each cleaning lasted 10 min. Then the substrates were dried with nitrogen flowing and transferred into the thermal evaporator without any treatment. C_{60} layer was deposited on the ITO with the speed of 0.3 Å s^{-1} under the vacuum of 3.2×10^{-6} mbar. To prepare ZnO - and SnO_2 -based substrate, ZnO and SnO_2 colloid solutions were spin-coated on O_2 plasma-treated ITO glass at 4000 rpm for 30 s, respectively, and then annealed at 150°C for 15 min in the air. For PCBM layer, a solution with the concentration of 20 mg mL^{-1} in CB was deposited on ITO and annealed at 100°C for 10 min. The $(MAPbI_3)_{0.4}(FASnI_3)_{0.6}$ solution (1.5 M) with the compositions of MAI (95.38 mg, 0.6 mmol), FAI (154.77 mg, 0.9 mmol), PbI_2 (276.61 mg, 0.6 mmol), SnI_2 (335.25 mg, 0.9 mmol), $Pb(SCN)_2$ (6.79 mg, 0.021 mmol), and SnF_2 (14.10 mg, 0.09 mmol) was prepared by mixing solvents (200 μL DMSO and 800 μL DMF) and stirred at room temperature for 4 h. After filtered with 0.45 μm PTFE filter, the precursor was coated onto the substrate at the speed of 2000 rpm for 5 s and then 5000 rpm for 40 s. DMF (70 μL) was dynamically spin-coated on C_{60} -based substrate at 5000 rpm for 20 s before depositing perovskite layer to improve the wetting property. Chlorobenzene (CB) (250 μL) was dropped at the center of the spinning substrate 20 s before the end of spin coating. Subsequently, the films were annealing at 80°C for 20 min. After cooling down to room temperature, the hole/electron transport layer was deposited on the perovskite at the speed of 3000 rpm for 30 s and then annealing at 80°C for 2 min. The hole transport material (PolyTPD, PTAA, P3HT, and PDCBT) was dissolved in CB with the concentration of 10 mg mL^{-1} and stirred overnight. The BCP solution was dissolved in isopropanol with a

concentration of 1.5 mg mL^{-1} . Finally, the devices with an area of 0.106 cm^2 were fabricated after the sequential deposition of 10 nm MoO_3 and 100 nm Ag.

Characterization: Surface morphology of the perovskite films was characterized with scanning electron microscopy (SEM) images by a FEI Helios NanoLab 660 apparatus with an acceleration voltage of 15 kV. XRD patterns were taken from a Panalytical X'pert powder diffractometer with filtered $Cu K\alpha$ radiation ($\lambda = 1.54178 \text{ Å}$) and an X'Celerator solid-state stripe detector. The XPS measurements were carried on using a Scienta ESCA 200 spectrometer with Al $K\alpha$ X-ray source (1486.6 eV) and a hemispherical electron energy analyzer (SES-200) under 5×10^{-10} mbar. $J-V$ characteristics were measured with a Keithley source measurement unit and a Newport Sol3A solar simulator, which could provide illumination with an AM1.5G spectrum and light intensity of 100 mW cm^{-2} . The light intensity was calibrated with a standard crystalline Si device. EQE spectra were obtained using an EQE measurement system assembled by Enli Technology (Taiwan). The FTPS was collected by reconstructed Vertex 70 FTIR spectrometer (Bruker Optics GmbH) equipped with an amplifier (Femto DLPCA-200) to increase the photocurrent. PLQY was calculated from the absolute PL measurements with integrating sphere, a 405 nm laser diode as the excitation source was adopted, and the laser intensity was altered by a step beam attenuator. The intensity of 1 sun illumination was adjusted to the photoflux equivalent to the overlap of bandgap (1.27 eV) and AM1.5G spectrum ($2.37 \times 10^{21} \text{ m}^{-2} \text{ s}^{-1}$). The optical fiber was used to connect the sphere and a silicon CCD array detector; a 420 nm filter was used to increase the integrated time. The setup was calibrated with a halogen lamp with specific spectral irradiance. The M-S plot was measured by the Zahner Zennium Pro potentiostat with the AC perturbation of 10 mV and 10 kHz in the dark and N_2 atmosphere.

Supporting Information

Supporting Information is available from the Wiley Online Library or from the author.

Acknowledgements

K.Z. and W.M. are grateful for the financial support from the China Scholarship Council (CSC). J.G.C. gratefully acknowledges the financial support from the Deutscher Akademischer Austausch Dienst (DAAD) through a doctoral scholarship. The authors also gratefully acknowledge the grants "ELF-PV—Design and development of solution processed functional materials for the next generations of PV technologies" (grant no. 44-6521a/20/4) and "Solar Factory of the Future" (FKZ 20.2-3410.5-4-5) by the Bavarian State Government. C.J.B. gratefully acknowledges the financial support through the Bavarian Initiative "Solar Technologies go Hybrid" (SolTech), the DFG—SFB953 (project no. 182849149), DFG—GRK2495 (ITRG2495), and the DFG—INST 90/917-1 FUGG. Q.X. acknowledges the funding by the Natural Science Foundation of China (grant no. 51803060), the Science and Technology Program of Guangdong Province, China (grant no. 2018A030313045), and the Science and Technology Program of Guangzhou, China (grant no. 201904010147).

Open access funding enabled and organized by Projekt DEAL. [Correction added on March 17, 2022, after first online publication: Projekt DEAL funding statement and a project number have been added.]

Conflict of Interest

The authors declare no conflict of interest.

Data Availability Statement

The data that supports the findings of this study are available in the supplementary material of this article.

Keywords

energy-level alignment, energy loss, interface, low-bandgap perovskite, Pb/Sn narrow-bandgap perovskite, transporting layer, trap density

Received: October 26, 2021

Published online: December 2, 2021

- [1] A. Kojima, K. Teshima, Y. Shirai, T. Miyasaka, *J. Am. Chem. Soc.* **2009**, 131, 6050.
- [2] The National Renewable Energy Laboratory (NREL), <https://www.nrel.gov/pv/cell-efficiency.html> (accessed: 2021).
- [3] G. E. Eperon, T. Leijtens, K. A. Bush, R. Prasanna, T. Green, J. T.-W. Wang, D. P. McMeekin, G. Volonakis, R. L. Milot, R. May, A. Palmstrom, D. J. Slotcavage, R. A. Belisle, J. B. Patel, E. S. Parrott, R. J. Sutton, W. Ma, F. Moghadam, B. Conings, A. Babayigit, H.-G. Boyen, S. Bent, F. Giustino, L. M. Herz, M. B. Johnston, M. D. McGehee, H. J. Snaith, *Science* **2016**, 354, 861.
- [4] N.-G. Park, K. Zhu, *Nat. Rev. Mater.* **2020**, 5, 333.
- [5] M. Cai, Y. Wu, H. Chen, X. Yang, Y. Qiang, L. Han, *Adv. Sci.* **2017**, 4, 1600269.
- [6] K. Xiao, R. Lin, Q. Han, Y. Hou, Z. Qin, H. T. Nguyen, J. Wen, M. Wei, V. Yeddu, M. I. Saidaminov, Y. Gao, X. Luo, Y. Wang, H. Gao, C. Zhang, J. Xu, J. Zhu, E. H. Sargent, H. Tan, *Nat. Energy* **2020**, 5, 870.
- [7] D. Zhao, Y. Yu, C. Wang, W. Liao, N. Shrestha, C. R. Grice, A. J. Cimaroli, L. Guan, R. J. Ellingson, K. Zhu, X. Zhao, R.-G. Xiong, Y. Yan, *Nat. Energy* **2017**, 2, 17018.
- [8] F. Hao, C. C. Stoumpos, R. P. H. Chang, M. G. Kanatzidis, *J. Am. Chem. Soc.* **2014**, 136, 8094.
- [9] M. T. Klug, R. L. Milot, J. B. Patel, T. Green, H. C. Sansom, M. D. Farrar, A. J. Ramadan, S. Martani, Z. Wang, B. Wenger, J. M. Ball, L. Langshaw, A. Petrozza, M. B. Johnston, L. M. Herz, H. J. Snaith, *Energy Environ. Sci.* **2020**, 13, 1776.
- [10] F. Zuo, S. T. Williams, P.-W. Liang, C.-C. Chueh, C.-Y. Liao, A. K. Y. Jen, *Adv. Mater.* **2014**, 26, 6454.
- [11] W. Liao, D. Zhao, Y. Yu, N. Shrestha, K. Ghimire, C. R. Grice, C. Wang, Y. Xiao, A. J. Cimaroli, R. J. Ellingson, N. J. Podraza, K. Zhu, R.-G. Xiong, Y. Yan, *J. Am. Chem. Soc.* **2016**, 138, 12360.
- [12] D. Ricciarelli, D. Meggiolaro, F. Ambrosio, F. De Angelis, *ACS Energy Lett.* **2020**, 5, 2787.
- [13] S. Gupta, D. Cahen, G. Hodes, *J. Phys. Chem. C* **2018**, 122, 13926.
- [14] J. Tong, Z. Song, D. H. Kim, X. Chen, C. Chen, A. F. Palmstrom, P. F. Ndione, M. O. Reese, S. P. Dunfield, O. G. Reid, J. Liu, F. Zhang, S. P. Harvey, Z. Li, S. T. Christensen, G. Teeter, D. Zhao, M. M. Al-Jassim, M. F. A. M. van Hest, M. C. Beard, S. E. Shaheen, J. J. Berry, Y. Yan, K. Zhu, *Science* **2019**, 364, 475.
- [15] X. Zhou, L. Zhang, X. Wang, C. Liu, S. Chen, M. Zhang, X. Li, W. Yi, B. Xu, *Adv. Mater.* **2020**, 32, 1908107.
- [16] R. Lin, K. Xiao, Z. Qin, Q. Han, C. Zhang, M. Wei, M. I. Saidaminov, Y. Gao, J. Xu, M. Xiao, A. Li, J. Zhu, E. H. Sargent, H. Tan, *Nat. Energy* **2019**, 4, 864.
- [17] T. Jiang, Z. Chen, X. Chen, T. Liu, X. Chen, W. E. I. Sha, H. Zhu, Y. Yang, *Sol. RRL* **2020**, 4, 1900467.
- [18] D. Chi, S. Huang, M. Zhang, S. Mu, Y. Zhao, Y. Chen, J. You, *Adv. Funct. Mater.* **2018**, 28, 1804603.
- [19] M. Wei, K. Xiao, G. Walters, R. Lin, Y. Zhao, M. I. Saidaminov, P. Todorović, A. Johnston, Z. Huang, H. Chen, A. Li, J. Zhu, Z. Yang, Y.-K. Wang, A. H. Proppe, S. O. Kelley, Y. Hou, O. Voznyy, H. Tan, E. H. Sargent, *Adv. Mater.* **2020**, 32, 1907058.
- [20] M. Abdi-Jalebi, Z. Andaji-Garmaroudi, S. Cacovich, C. Stavrakas, B. Philippe, J. M. Richter, M. Alsari, E. P. Booker, E. M. Hutter, A. J. Pearson, S. Lilliu, T. J. Savenije, H. Rensmo, G. Divitini, C. Ducati, R. H. Friend, S. D. Stranks, *Nature* **2018**, 555, 497.
- [21] Y. Ogomi, A. Morita, S. Tsukamoto, T. Saitho, N. Fujikawa, Q. Shen, T. Toyoda, K. Yoshino, S. S. Pandey, T. Ma, S. Hayase, *J. Phys. Chem. Lett.* **2014**, 5, 1004.
- [22] S. Nakayashiki, H. Daisuke, Y. Ogomi, S. Hayase, *J. Photonics Energy* **2015**, 5, 057410.
- [23] J. Yuan, Y. Jiang, T. He, G. Shi, Z. Fan, M. Yuan, *Sci. China Chem.* **2019**, 62, 629.
- [24] D. P. McMeekin, S. Mahesh, N. K. Noel, M. T. Klug, J. Lim, J. H. Warby, J. M. Ball, L. M. Herz, M. B. Johnston, H. J. Snaith, *Joule* **2019**, 3, 387.
- [25] M. Liu, Z. Chen, Z. Chen, H.-L. Yip, Y. Cao, *Mater. Chem. Front.* **2019**, 3, 496.
- [26] H. Tan, A. Jain, O. Voznyy, X. Lan, F. P. García de Arquer, J. Z. Fan, R. Quintero-Bermudez, M. Yuan, B. Zhang, Y. Zhao, F. Fan, P. Li, L. N. Quan, Y. Zhao, Z.-H. Lu, Z. Yang, S. Hoogland, E. H. Sargent, *Science* **2017**, 355, 722.
- [27] Q. Jiang, Y. Zhao, X. Zhang, X. Yang, Y. Chen, Z. Chu, Q. Ye, X. Li, Z. Yin, J. You, *Nat. Photon.* **2019**, 13, 460.
- [28] N. Li, S. Tao, Y. Chen, X. Niu, C. K. Onwudinanti, C. Hu, Z. Qiu, Z. Xu, G. Zheng, L. Wang, Y. Zhang, L. Li, H. Liu, Y. Lun, J. Hong, X. Wang, Y. Liu, H. Xie, Y. Gao, Y. Bai, S. Yang, G. Brocks, Q. Chen, H. Zhou, *Nat. Energy* **2019**, 4, 408.
- [29] Y. Liu, S. Akin, L. Pan, R. Uchida, N. Arora, J. V. Milić, A. Hinderhofer, F. Schreiber, A. R. Uhl, S. M. Zakeeruddin, A. Hagfeldt, M. I. Dar, M. Grätzel, *Sci. Adv.* **2019**, 5, eaaw2543.
- [30] W. H. Nguyen, C. D. Bailie, E. L. Unger, M. D. McGehee, *J. Am. Chem. Soc.* **2014**, 136, 10996.
- [31] K. Lee, J. Kim, H. Yu, J. W. Lee, C.-M. Yoon, S. K. Kim, J. Jang, *J. Mater. Chem. A* **2018**, 6, 24560.
- [32] Y. Hou, X. Du, S. Scheiner, D. P. McMeekin, Z. Wang, N. Li, M. S. Killian, H. Chen, M. Richter, I. Levchuk, N. Schrenker, E. Spiecker, T. Stubhan, N. A. Luechinger, A. Hirsch, P. Schmuki, H.-P. Steinrück, R. H. Fink, M. Halik, H. J. Snaith, C. J. Brabec, *Science* **2017**, 358, 1192.
- [33] E. H. Jung, N. J. Jeon, E. Y. Park, C. S. Moon, T. J. Shin, T.-Y. Yang, J. H. Noh, J. Seo, *Nature* **2019**, 567, 511.
- [34] M. Stollerfoht, P. Caprioglio, C. M. Wolff, J. A. Márquez, J. Nordmann, S. Zhang, D. Rothhardt, U. Hörmann, Y. Amir, A. Redinger, L. Kegelmann, F. Zu, S. Albrecht, N. Koch, T. Kirchartz, M. Saliba, T. Unold, D. Neher, *Energy Environ. Sci.* **2019**, 12, 2778.
- [35] Y. Liu, M. Bag, L. A. Renna, Z. A. Page, P. Kim, T. Emrick, D. Venkataraman, T. P. Russell, *Adv. Energy Mater.* **2016**, 6, 1501606.
- [36] A. Rajagopal, P.-W. Liang, C.-C. Chueh, Z. Yang, A. K. Y. Jen, *ACS Energy Lett.* **2017**, 2, 2531.
- [37] C. Liu, W. Li, H. Li, C. Zhang, J. Fan, Y. Mai, *Nanoscale* **2017**, 9, 13967.
- [38] Z. Yu, Z. Yang, Z. Ni, Y. Shao, B. Chen, Y. Lin, H. Wei, Z. J. Yu, Z. Holman, J. Huang, *Nat. Energy* **2020**, 5, 657.
- [39] C. C. Stoumpos, C. D. Malliakas, M. G. Kanatzidis, *Inorg. Chem.* **2013**, 52, 9019.
- [40] W. Ke, I. Spanopoulos, Q. Tu, I. Hadar, X. Li, G. S. Shekhwat, V. P. Dravid, M. G. Kanatzidis, *J. Am. Chem. Soc.* **2019**, 141, 8627.
- [41] T. Leijtens, R. Prasanna, A. Gold-Parker, M. F. Toney, M. D. McGehee, *ACS Energy Lett.* **2017**, 2, 2159.
- [42] G. Xu, P. Bi, S. Wang, R. Xue, J. Zhang, H. Chen, W. Chen, X. Hao, Y. Li, Y. Li, *Adv. Funct. Mater.* **2018**, 28, 1804427.
- [43] H. Tang, Y. Shang, W. Zhou, Z. Peng, Z. Ning, *Sol. RRL* **2019**, 3, 1800256.

- [44] O. Almora, C. I. Cabrera, J. Garcia-Cerrillo, T. Kirchartz, U. Rau, C. J. Brabec, *Adv. Energy Mater.* **2021**, 11.
- [45] P. Caprioglio, M. Stolterfoht, C. M. Wolff, T. Unold, B. Rech, S. Albrecht, D. Neher, *Adv. Energy Mater.* **2019**, 9, 1901631.
- [46] T. Kirchartz, J. A. Márquez, M. Stolterfoht, T. Unold, *Adv. Energy Mater.* **2020**, 10, 1904134.
- [47] U. Rau, *Phys. Rev. B* **2007**, 76.
- [48] G. D. Cody, *J. Non-Cryst. Solids* **1992**, 141, 3.
- [49] S. R. Johnson, T. Tiedje, *J. Appl. Phys.* **1995**, 78, 5609.
- [50] M. Troviano, K. Taretto, *Sol. Energy Mater. Sol. Cells* **2011**, 95, 821.
- [51] W. Tress, *Adv. Energy Mater.* **2017**, 7, 1602358.
- [52] S. Mahesh, J. M. Ball, R. D. J. Oliver, D. P. McMeekin, P. K. Nayak, M. B. Johnston, H. J. Snaith, *Energy Environ. Sci.* **2020**, 13, 258.
- [53] J. Jean, T. S. Mahony, D. Bozyigit, M. Sponseller, J. Holovsky, M. G. Bawendi, V. Bulović, *ACS Energy Lett.* **2017**, 2, 2616.
- [54] A. R. Bowman, M. T. Klug, T. A. S. Doherty, M. D. Farrar, S. P. Senanayak, B. Wenger, G. Divitini, E. P. Booker, Z. Andaji-Garmaroudi, S. Macpherson, E. Ruggeri, H. Sirringhaus, H. J. Snaith, S. D. Stranks, *ACS Energy Lett.* **2019**, 4, 2301.
- [55] N. B. Kotadiya, H. Lu, A. Mondal, Y. Ie, D. Andrienko, P. W. M. Blom, G.-J. A. H. Wetzelaer, *Nat. Mater.* **2018**, 17, 329.
- [56] O. Almora, C. Aranda, E. Mas-Marzá, G. Garcia-Belmonte, *Appl. Phys. Lett.* **2016**, 109.
- [57] C. van Opdorp, *Solid-State Electron.* **1968**, 11, 397.
- [58] J.-F. Guillemoles, T. Kirchartz, D. Cahen, U. Rau, *Nat. Photon.* **2019**, 13, 501.
- [59] T. S. Sherkar, C. Momblona, L. Gil-Escrig, H. J. Bolink, L. J. A. Koster, *Adv. Energy Mater.* **2017**, 7.
- [60] V. M. Le Corre, M. Stolterfoht, L. Perdigón Toro, M. Feuerstein, C. Wolff, L. Gil-Escrig, H. J. Bolink, D. Neher, L. J. A. Koster, *ACS Appl. Energy Mater.* **2019**, 2, 6280.
- [61] T. S. Sherkar, C. Momblona, L. Gil-Escrig, J. Avila, M. Sessolo, H. J. Bolink, L. J. A. Koster, *ACS Energy Lett.* **2017**, 2, 1214.